RANS Approach to 2D Shear Mixing Flow

V. Vinay Kumar

Contact: `vinaykumardaproject@gmail.com`

07 August 2025

Abstract

This report presents a numerical investigation of the 2D Delville shear layer, a benchmark case for validating turbulence models in computational fluid dynamics (CFD). Simulations were conducted using the Reynolds-Averaged Navier-Stokes (RANS) framework with the Spalart–Allmaras (SA) turbulence model in ANSYS Fluent to evaluate its ability to capture shear layer dynamics and turbulent diffusion. Mesh configurations ranging from 29K to 116K cells were used to assess grid sensitivity. Results were compared against NASA's Turbulence Modeling Resource experimental data, focusing on axial velocity profiles and turbulent viscosity distributions. Good agreement was observed in near-field velocity profiles, but discrepancies emerged in the far-field, with velocity overpredicted near the plate tip and underpredicted downstream. Finer mesh resolution proved critical for resolving turbulent mixing and velocity decay. These findings highlight the SA model's strengths and limitations in shear-dominated flows, showing that while it performs well near the origin, accurate downstream predictions require finer grids.

Introduction

Turbulent mixing layers are critical in engineering applications like aerospace and combustion systems due to their role in momentum and mass transfer. The Delville shear layer, a benchmark case, is ideal for validating turbulence models [2]. This study numerically investigates the 2D Delville shear layer using the Reynolds-Averaged Navier-Stokes (RANS) framework with the Spalart-Allmaras (SA) model in ANSYS Fluent [1, 4]. It evaluates the model's ability to capture shear layer instabilities and turbulent diffusion, using varied mesh resolutions to assess grid sensitivity. Results are compared with NASA's Delville shear layer data [3], providing insights into the SA model's performance in computational fluid dynamics (CFD).

1 Geometrical Modeling

The 2D Mixing layer is computationally performed in the geometry as dimensions are shown in the Fig. 1. The upper inlet is 150 mm wide in the positive y-direction, and the lower inlet of the same dimension in the negative y-direction. A plate with a thickness of 3 mm and a length of 300 mm tapers from a thickness of 3 mm at x = -50 mm to 0.3 mm at x = 0 mm. To simplify the discretization process, a sharp tip is modeled at x = 0 mm. This plate separates the upper and lower fluids. The upper inlet is positioned 550

mm upstream of the plate tip, while the lower inlet is located 300 mm upstream of the same reference point. The domain extends 1200 mm in the x-direction from the tip. The walls located along the x-axis at y = 0 mm of both inlets are treated as no-slip, adiabatic solid boundaries, while the other walls are treated as slip walls.

A 2D computational domain was constructed using ANSYS DesignModeler software, based on the dimensions and modifications described in the preceding paragraph and illustrated in Fig. 1. The finalized geometry of the CFD model is presented in Fig. 2.
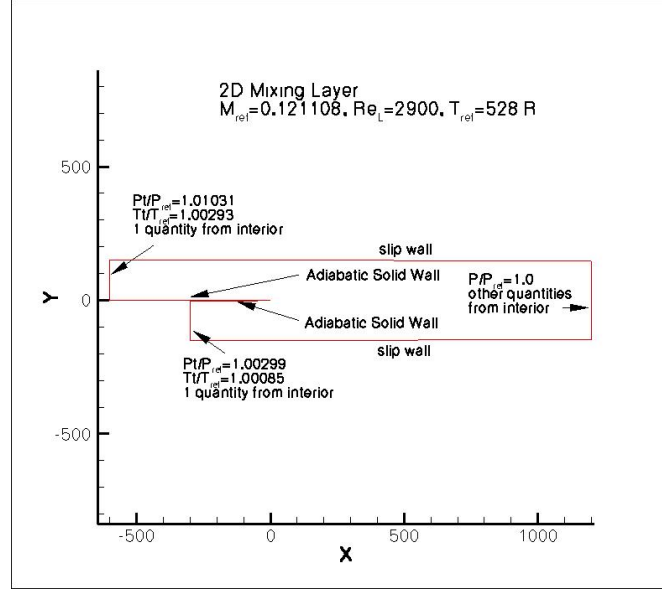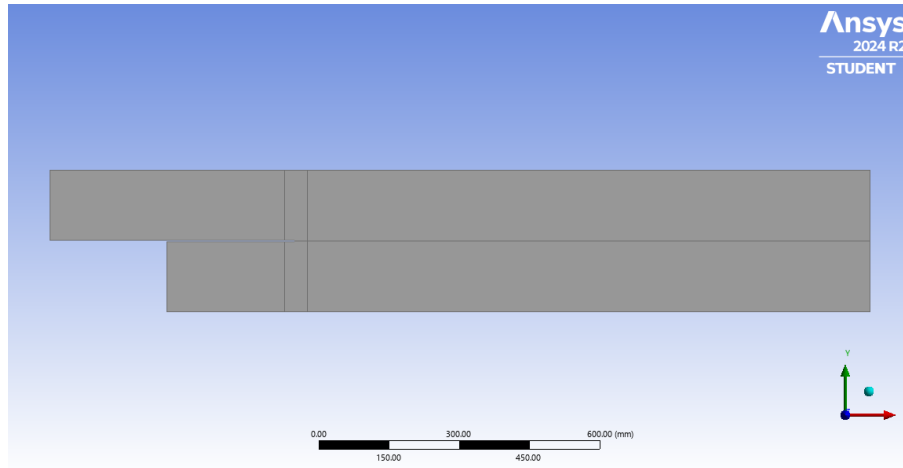

Figure 1: Geometry dimension [3, 2]

Figure 2: Computational 2D Domain designed in Ansys DesignModular

2 Methodology

2.1 Numerical Modeling

The computational analysis was carried out using the ANSYS Fluent Student Version, a widely used CFD solver that supports a range of turbulence models and numerical

schemes. The simulation was based on the Reynolds-Averaged Navier–Stokes (RANS) equations along with the Spalart-Allmaras turbulence model, which are the foundation for most industrial turbulence modeling due to their balance of accuracy and computational efficiency.

RANS Equations in ANSYS Fluent

The Reynolds-Averaged Navier–Stokes (RANS) equations are derived by decomposing instantaneous quantities into mean and fluctuating components and applying Reynolds averaging. The following equations are solved in this computational case [1]:

Continuity Equation

$$\frac{\partial \rho}{\partial t} + \nabla \cdot (\rho \vec{v}) = 0 \tag{1}$$

Momentum Equation

$$\frac{\partial}{\partial t}(\rho \vec{v}) + \nabla \cdot (\rho \vec{v} \vec{v}) = -\nabla p + \rho \vec{g} + \vec{F} \tag{2}$$

Here:

- $\rho \vec{g}$ is the gravitational body force,

- $\vec{F}$ is the external body force,

- p is the static pressure.

Energy Equation

$$\frac{\partial}{\partial t}(\rho E) + \nabla \cdot (\vec{v}(\rho E + p)) = -\nabla \cdot \left(\sum_j h_j J_j \right) + S_h \tag{3}$$

Where:

- E is the total mean energy per unit mass, defined as $E = e + \frac{1}{2}|\vec{v}|^2$, where e is internal energy and $\vec{v}$ is velocity,

- ρ is the fluid density,

- p is the pressure,

- $\vec{v}$ is the velocity vector,

- h_j is the specific enthalpy of species j,

- J_j is the diffusive flux of species j,

- S_h is the volumetric energy source term (e.g., chemical reaction heat, radiation),

- k is the thermal conductivity,

- $\overline{T}$ is the mean temperature,

- Φ represents viscous dissipation and other mechanical or thermal source terms.

Spalart-Allmaras Turbulence Model

Transport Equation for the Spalart-Allmaras Model

The Spalart-Allmaras model is a one-equation turbulence model that solves a transport equation for the modified turbulent viscosity, $\tilde{\nu}$ [4]. The transport equation, as implemented in ANSYS Fluent, is given by:

$$\frac{\partial}{\partial t}(\rho\tilde{\nu}) + \frac{\partial}{\partial x_j}(\rho\tilde{\nu}u_j) = G_v + \frac{1}{\sigma_{\tilde{\nu}}}\left[\frac{\partial}{\partial x_j}\left((\mu + \rho\tilde{\nu})\frac{\partial\tilde{\nu}}{\partial x_j}\right) + C_{b2}\rho\left(\frac{\partial\tilde{\nu}}{\partial x_j}\right)^2\right] - Y_v + S_{\tilde{\nu}} \quad (4)$$

where ρ is the density, u_j is the velocity component, G_v is the production of turbulent viscosity, Y_v is the destruction of turbulent viscosity, $\sigma_{\tilde{\nu}}$ and C_{b2} are constants, and $S_{\tilde{\nu}}$ is a user-defined source term.

Modeling the Turbulent Viscosity

The turbulent viscosity μ_t is computed from the modified turbulent viscosity $\tilde{\nu}$ as:

$$\mu_t = \rho\tilde{\nu}f_{v1} \quad (5)$$

where the viscous damping function f_{v1} is defined as:

$$f_{v1} = \frac{\chi^3}{\chi^3 + C_{v1}^3}, \quad \chi = \frac{\tilde{\nu}}{\nu} \quad (6)$$

Here, $\nu = \mu/\rho$ is the molecular kinematic viscosity, and C_{v1} is a constant.

Modeling the Turbulent Production

The production term G_v in the transport equation is modeled as:

$$G_v = C_{b1}\rho\tilde{S}\tilde{\nu} \quad (7)$$

where C_{b1} is a constant, and $\tilde{S}$ is the modified strain rate magnitude, defined as:

$$\tilde{S} = S + \frac{\tilde{\nu}}{\kappa^2 d^2}f_{v2} \quad (8)$$

with the strain rate magnitude $S = \sqrt{2\Omega_{ij}\Omega_{ij}}$, where Ω_{ij} is the mean rate-of-rotation tensor, κ is the von Kármán constant, d is the distance to the nearest wall, and the function f_{v2} is:

$$f_{v2} = 1 - \frac{\chi}{1 + \chi f_{v1}} \quad (9)$$

Modeling the Turbulent Destruction

The destruction term Y_v is modeled as:

$$Y_v = C_{w1}\rho f_w\left(\frac{\tilde{\nu}}{d}\right)^2 \quad (10)$$

where C_{w1} is a constant, and the function f_w is defined as:

$$f_w = g\left(\frac{1 + C_{w3}^6}{g^6 + C_{w3}^6}\right)^{1/6}, \quad g = r + C_{w2}(r^6 - r), \quad r = \frac{\tilde{\nu}}{\tilde{S}\kappa^2 d^2} \quad (11)$$

Here, C_{w2} and C_{w3} are constants.

Model Constants

The Spalart-Allmaras model uses the following constants, as specified in ANSYS Fluent [1]:

$$C_{b1} = 0.1355, \quad C_{b2} = 0.622, \quad \sigma_{\tilde{\nu}} = \frac{2}{3}, \quad C_{v1} = 7.1,$$

$$C_{w1} = \frac{C_{b1}}{\kappa^2} + \frac{1 + C_{b2}}{\sigma_{\tilde{\nu}}}, \quad C_{w2} = 0.3, \quad C_{w3} = 2.0, \quad \kappa = 0.41 \tag{12}$$

Wall Boundary Conditions

At solid walls, the modified turbulent viscosity $\tilde{\nu}$ is set to zero to enforce the no-slip condition:

$$\tilde{\nu} = 0 \quad \text{at walls} \tag{13}$$

This boundary condition ensures that the turbulent viscosity is zero at the wall, consistent with the physical behavior of the flow.

Model constants and functions such as $C_{b1}, C_{b2}, C_{w1}, \sigma, \kappa, f_w, f_{t1}, f_{t2}$ are defined in Fluent's documentation and tuned for aerodynamic flows.

2.2 Boundary Conditions

The boundary conditions for the ANSYS Fluent simulation are defined as follows:

- **Inlets:**

    - `inlet_1` has a velocity magnitude of 41.54 m/s and a temperature of 300 K.
    - `inlet_2` has a velocity magnitude of 22.4 m/s and a temperature of 300 K.
    - Both inlets use the *Magnitude, Normal to Boundary* method for velocity specification.
    - Turbulence is defined using the *Intensity and Hydraulic Diameter* method, with a turbulence intensity of 0.3% and a hydraulic diameter of 260.8696 mm.

- **Outlet:**

    - The outlet is set with a gauge pressure of 0 Pa.
    - The backflow total temperature is specified as 300 K.
    - A turbulent viscosity ratio of 10 is used.
    - Flow direction is specified as *Normal to Boundary*.

- **Walls:**

    - All walls are assigned aluminum as the material.
    - Thermal boundary condition is set to a heat flux of 0 W/m^2.
    - Wall motion is stationary.
    - `top_slip_wall` and `bottom_slip_wall` use a specified shear condition of 0 Pa.
    - `top_wall`, `bottom_wall`, `top_taper`, and `bottom_taper` use no-slip conditions.

- Wall roughness height is 0 mm.
- Roughness constant is set to 0.5 for no-slip walls and 0 for slip walls.
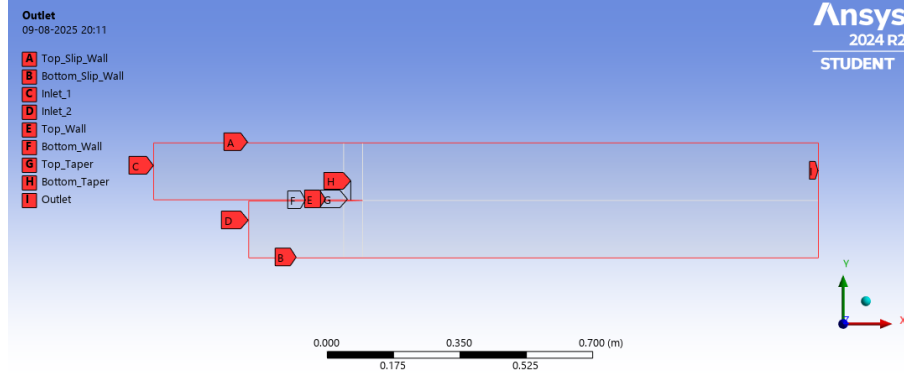- Convective augmentation factor is set to 1 for all walls.

Figure 3: Boundary conditions

2.3   Mesh

To enable localized refinement and region-specific modeling, the computational domain is divided into three distinct zones—Zone 1, Zone 2, and Zone 3 as illustrated in Fig. 4. Each zone is further divided into upper (U) and lower (L) regions to capture geometric and flow-specific variations with greater fidelity. This division accounts for differences in fluid velocity between the upper and lower regions, which necessitate adjustments in the first cell height and mesh bias to achieve the desired y^+. In CFD simulations, the non-dimensional wall distance y^+ is essential for accurately resolving near-wall turbulence and estimating wall shear stress. It is defined as:

$$y^+ = \frac{y u_\tau}{\nu} \tag{14}$$

Where: 'y' is the distance from the wall, $u_\tau = \sqrt{\tau_w / \rho}$ is the friction velocity,

Table 1: Mesh configuration.

S.no	Name	Zone 1U	Zone 1L	Zone 2U	Zone 2L	Zone 3U	Zone 3L	Cell count
1	Base	53×53	53×32	53×21	53×21	52×210	52×210	29K
2	Medium	75×75	75×45	75×10	75×10	75×300	75×300	58K
3	Fine	106×106	106×64	106×42	106×42	106×424	106×424	116K

All no-slip wall boundaries are resolved with $y^+ \approx 1$, ensuring adequate near-wall resolution for turbulence modeling and accurate boundary layer representation. The mesh is biased toward the tip of the plate along the x-axis up to x = −50 mm for Zones 1L and 1U. Zones 2U and 2L feature a consistently uniform mesh along the x−axis. In contrast, Zones 3U and 3L employ a biased mesh toward the tip of the plate. Additionally, the mesh is biased toward the slip wall in Zones 1L, 1U, 2U, and 2L, as shown in Fig. 5. The bias factor is varied between the upper (U) and lower (L) regions to accommodate

$y^+ \approx 1$, based on local velocity profiles. This variation directly influences the wall shear stress distribution along the surface.

The mesh configurations for three levels of resolution, Base, Medium, and Fine, are summarized in Table 1. These configurations reflect increasing levels of refinement, with corresponding increases in cell count to support higher accuracy in simulations.
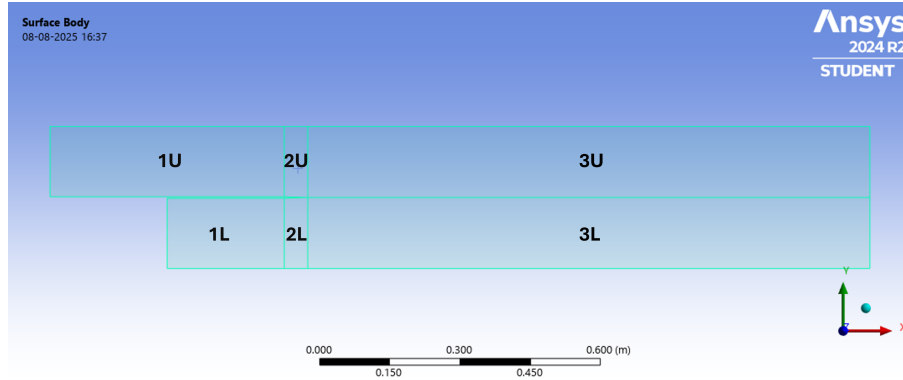

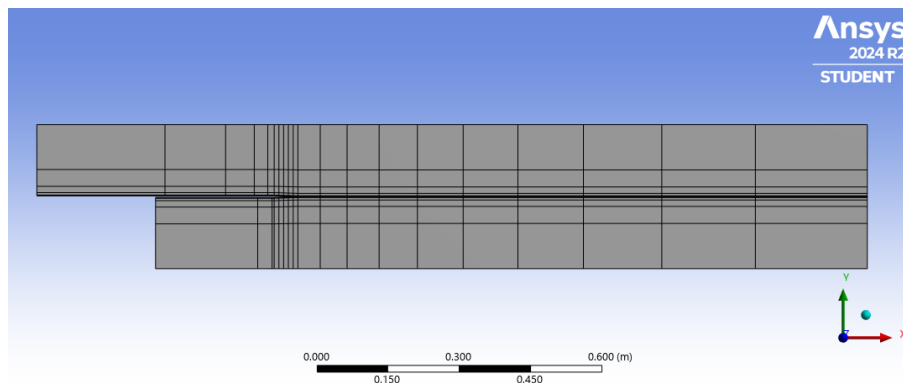Figure 4: Partitioned domain showing Zones 1, 2, and 3, each representing different flow regimes or boundary conditions.

Figure 5: Mesh Biasing
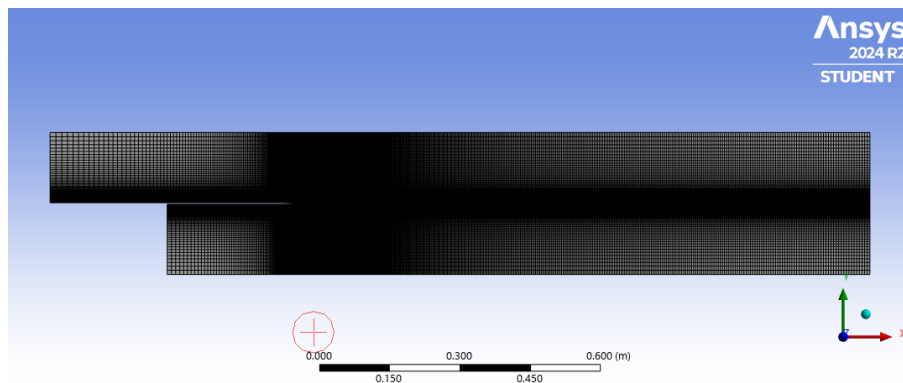
Figure 6: Mesh of fine resolution.

2.4   Grid Independency

A grid independence study was conducted to ensure the consistency of simulation results across varying mesh densities. Several mesh configurations, as presented in Table 1, were evaluated, each designed to maintain near-wall resolution with $y^+ \approx 1$ to accurately capture the viscous sublayer. The medium-resolution mesh, consisting of 58K cells, was selected based on the stability of key flow quantities. Specifically, the net mass flow rate ($\dot{m}$) was found to be nearly zero, as shown in Fig. 7, and successive mesh refinements showed minimal variation in flow parameters, as shown in Fig. 11. This is illustrated in Fig. 8, 9, 10, which shows that the centerline axial variation of x-velocity, y-velocity, and turbulent viscosity for both the medium (58K cells) and fine (116K cells) meshes is nearly identical. Further analysis revealed that the base mesh configuration underpredicted the diffusion of turbulence, resulting in a noticeably lower u-velocity magnitude compared to the medium and fine meshes. This discrepancy is attributed to the elevated turbulent viscosity values observed along the axial direction in the base mesh case, which artificially dampen the velocity field. Consequently, the base mesh fails to accurately capture the turbulent transport characteristics, reinforcing the need for medium to finer resolution to ensure reliable flow predictions. Medium resolution is chosen, yielding results comparable to fine, while being computationally efficient. These findings confirm mesh convergence and validate the choice of the medium-resolution grid.
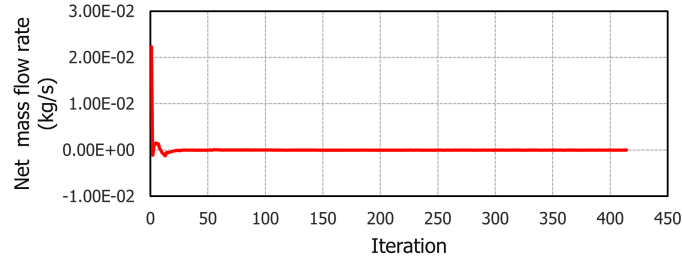

Figure 7: Variation of net mass flow rate ($\dot{m}$, kg/s) over iterations.
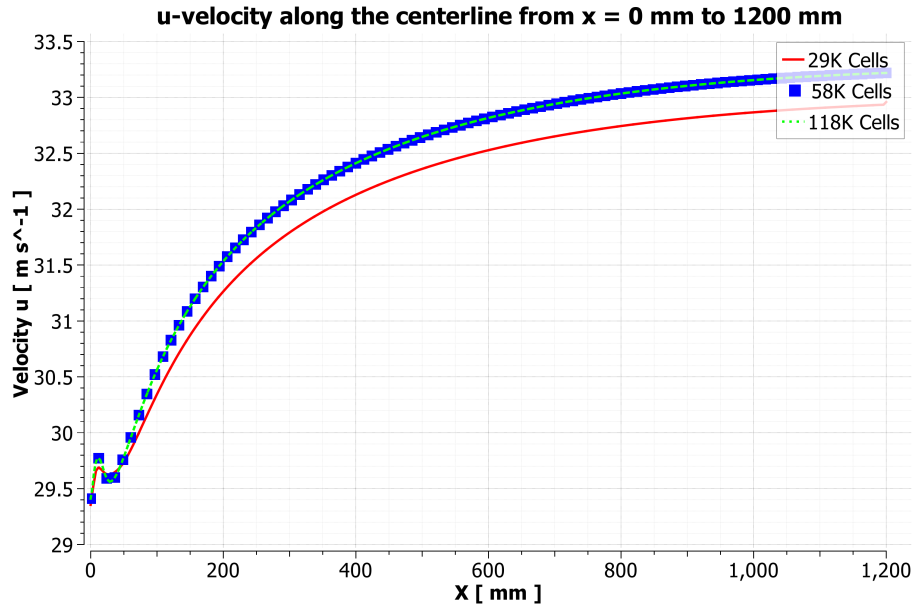

Figure 8: Comparison of centerline U-velocity profiles for different mesh configurations used in the grid independence study.
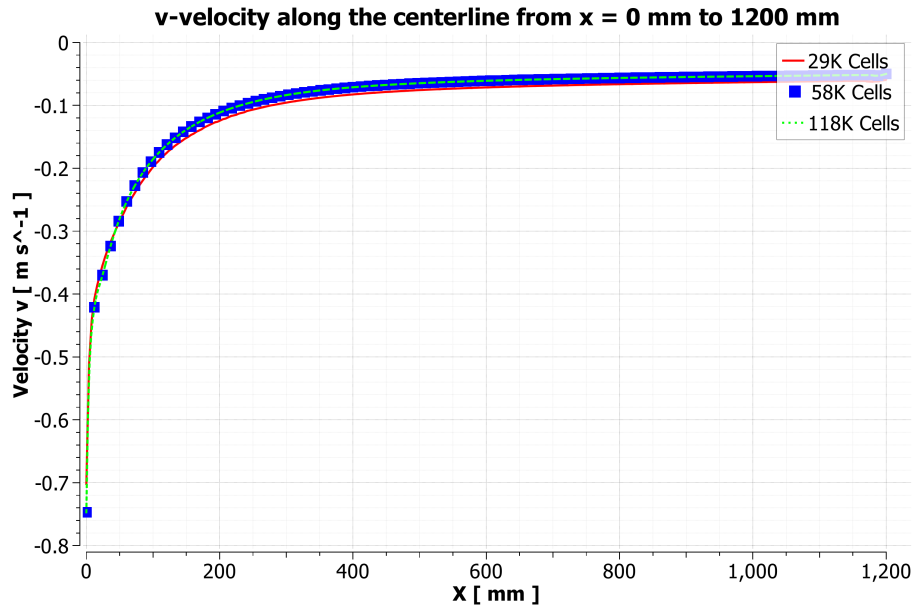
Figure 9: Comparison of centerline V-velocity profiles for different mesh configurations used in the grid independence study.
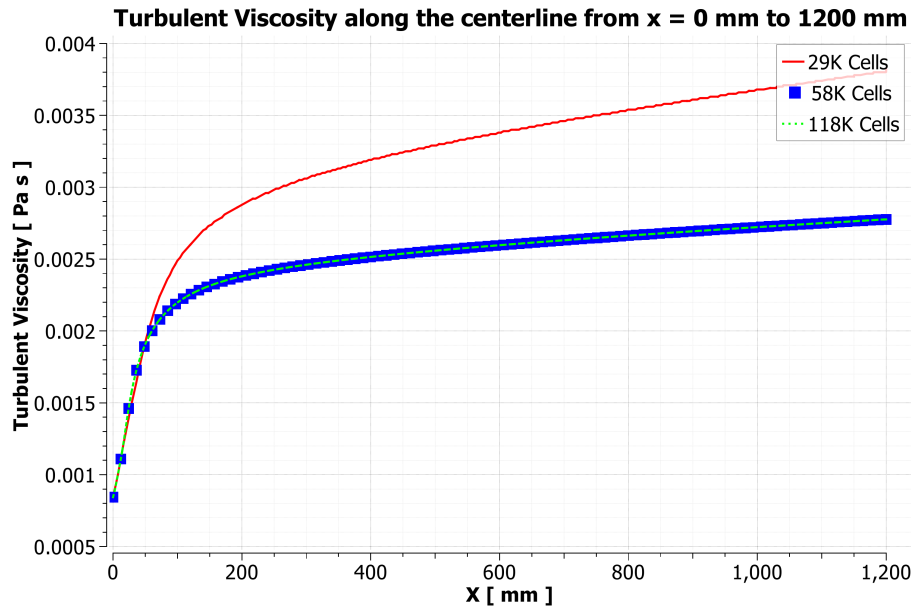

Figure 10: Comparison of centerline turbulent viscosity for different mesh configurations used in the grid independence study.
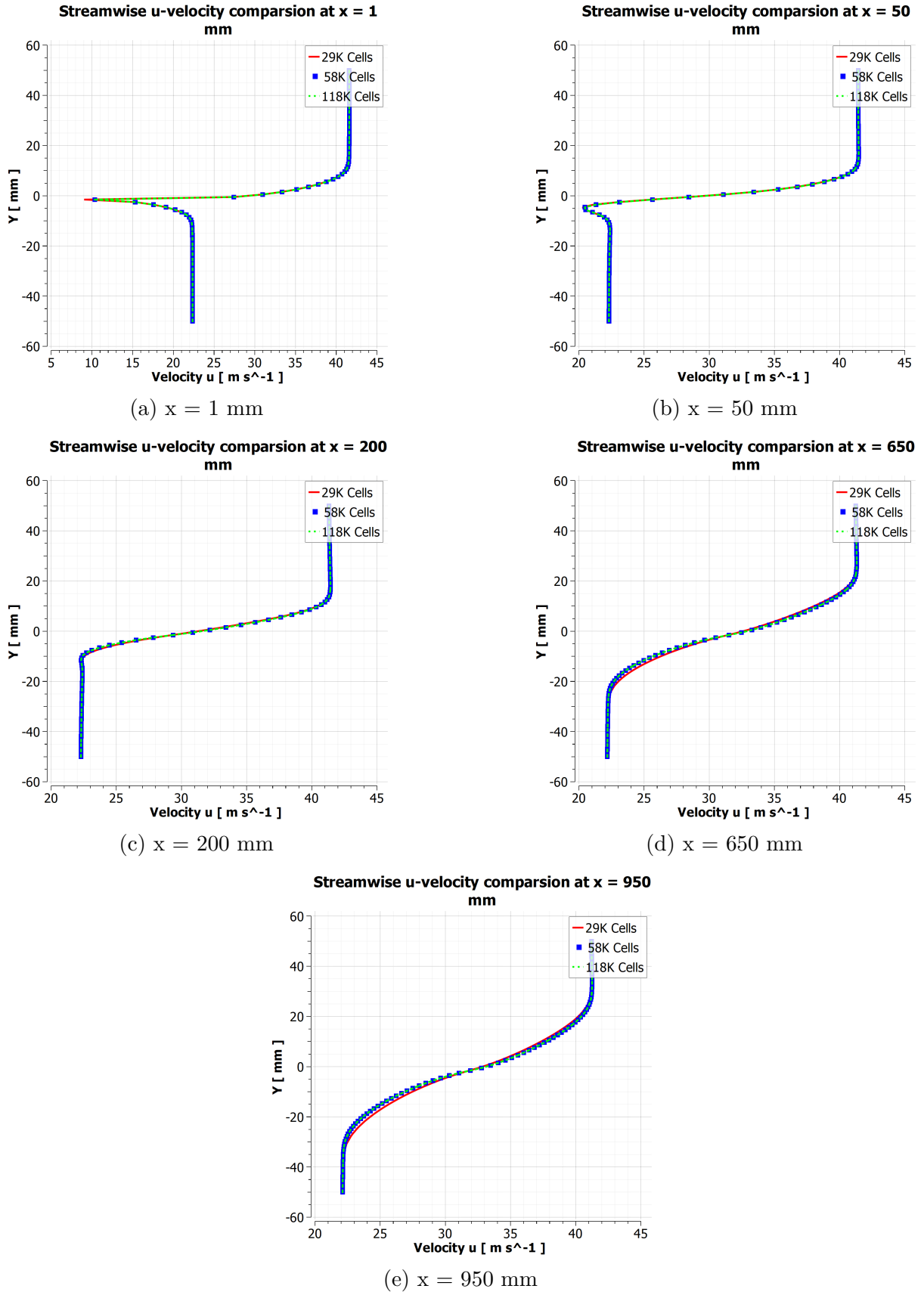
(a) x = 1 mm

(b) x = 50 mm

(c) x = 200 mm

(d) x = 650 mm

(e) x = 950 mm

Figure 11: Streamwise u-velocity profile at various x-location for different mesh configuration.

3   Results

(a) x = 1 mm

(b) x = 50 mm
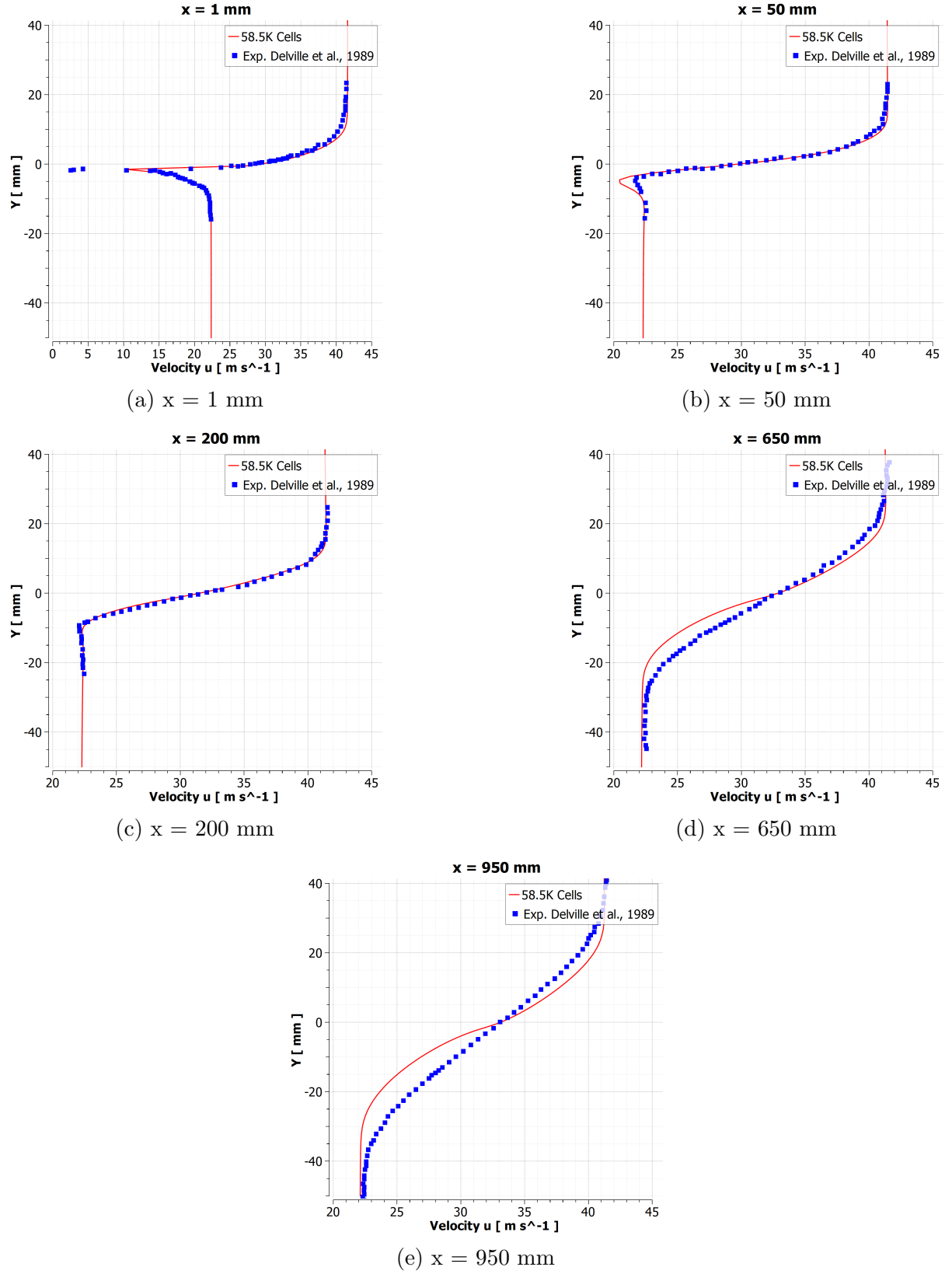

(c) x = 200 mm

(d) x = 650 mm

(e) x = 950 mm

Figure 12: Comparison of streamwise u-velocity profile at various x-location with experiment results of Delville et al. (1989).

Computational streamwise velocity profiles at x = 1, 50, 200, 650, and 950 mm from the tip of the splitter plate are compared with the experimental results, and they are in good agreement with the experimental results of Delville et al. (1989). At x = 1 mm, x-velocity is similar profile for both cases except at the y = −1.5 mm, where the tip of the plate lies, as shown in Fig. 12a. The observed difference can be attributed to two primary factors. First, limitations in experimental measurement techniques may introduce uncertainties, particularly in regions with steep gradients or fine geometric features. Second, the computational model approximates the tip geometry as perfectly sharp, whereas the actual experimental setup features a tip with a finite thickness of approximately 0.3 mm. This geometric simplification can significantly influence local flow behavior, especially near the tip, where small changes in contour can alter separation, vortex formation, and pressure distribution.

At x = 50 mm, the velocity profiles of experiment and computation overlap each other, except at the y-location where the tip lies; similar behavior was seen in the x = 1 mm, as shown in Fig. 12b. The computational cases underpredicted the x-velocity by nearly 2%, suggesting that the SA model captures the downstream mixing reasonably well but may slightly dampen the momentum transport. In contrast, it overpredicted in the case of x = 1 mm by 50%, indicating a stronger initial shear layer development in the simulation. These discrepancies highlight the sensitivity of the SA model to near-field gradients and tip-induced perturbations in shear-dominated flows.

At x = 200 mm, experiment and computational are overlapping with each other. The transition of velocity between two zones occurs linearly through a shear region, as shown in Fig. 12c. Whereas in the upstream velocity profiles, a velocity decrement is observed in the contact zone, whose profile shape resembles a wake velocity profile.

At downstream locations $x = 650$ mm and $x = 950$ mm, the velocity profiles exhibit a consistent trend in the simulation results. Specifically, the computational model slightly underpredicts the velocity in the region of low-speed fluid, typically associated with the entrainment and mixing of the slower stream. Conversely, in the region of higher-speed fluid, the simulation tends to overpredict the velocity magnitude. The velocity variation in the shear zone and also the region adjacent to the shear zone shows a polynomial variation; in contrast, it is linear in the case of the experiment, as shown in Fig. 12d, 12d. Kinetic energy of the flow in the computational case is higher than in the experimental case, which shows that the energy dissipation is lower in the computational case. This behavior suggests that the turbulence model may be overestimating the momentum transfer from the high-velocity stream into the mixing layer, while simultaneously underpredicting the diffusion and deceleration effects in the low-speed region. Such discrepancies are common in shear layer simulations, particularly when using eddy-viscosity-based models like Spalart–Allmaras, which may struggle to fully resolve anisotropic turbulence and large-scale vortical structures at far-field locations.

The boundary layer thickness over a flat surface is inversely proportional to the Reynolds number and directly proportional to the characteristic length scale. In the current case, the boundary layer developed over the top surface of the plate is thicker than that on the lower surface, even though the Reynolds number is higher for the top surface. However, its influence is of square root-order magnitude, and the length scale for the top surface is 250 mm greater than that of the lower surface, which ultimately leads to a higher boundary layer thickness.

Empirical measurements show that the boundary layer thickness δ_{99} on the top surface is $\delta_{99,top} = 17.1$ mm, while on the bottom surface it is around $\delta_{99,bottom} = 7.44$ mm. In the

computational case, using a reference length measured from the inlet to 10 mm upstream of the tip, the boundary layer thickness on the top surface is approximately $\delta_{99,top} = 15$ mm, and on the bottom surface it is about $\delta_{99,bottom} = 8.5$ mm, as shown in Fig. 13. These results further support the observation that the longer effective length scale on the top surface contributes significantly to the increased boundary layer thickness, even in the presence of a higher Reynolds number.
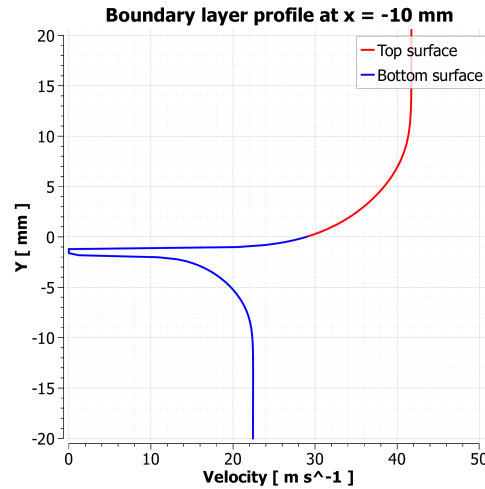

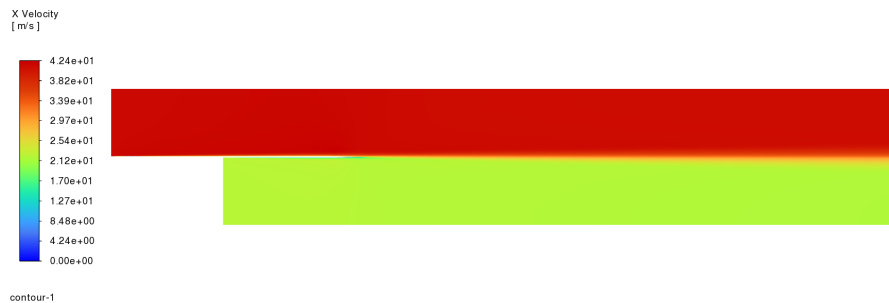Figure 13: Boundary layer profile over the top and bottom surfaces of the plate, which separates the flows.
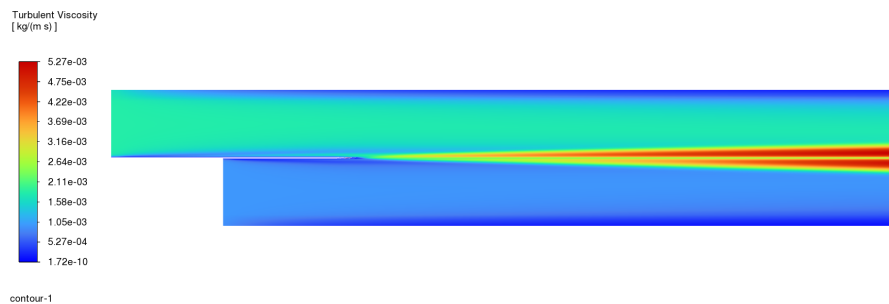

Figure 14: Contour of x-velocity

Figure 15: Contour of turbulent viscosity

The boundary layer thickness plays a significant role in influencing the distribution and magnitude of turbulent viscosity within a flow field. A thicker boundary layer generally indicates a more developed shear region, which can enhance turbulence production and mixing. From the contour images, it is evident that the turbulent viscosity adjacent to the bottom surface is approximately in order of 10^{-4}, whereas in the boundary region near the top surface, it reaches a higher value of about 10^{-3}, as shown in Fig. 15. This correlates with the observed difference in boundary layer thickness—where the top surface exhibits a thicker boundary layer. The increased thickness on the top surface allows for greater momentum exchange and turbulent eddy formation, thereby elevating the turbulent viscosity. In contrast, the thinner boundary layer on the bottom surface limits the extent of turbulent mixing, resulting in lower turbulent viscosity. These findings underscore the direct relationship between boundary layer development and turbulence intensity in wall-bounded flows.

In this study, the turbulent viscosity distribution is modeled using the Spalart–Allmaras (SA) turbulence model, which solves a transport equation for a modified turbulent kinematic viscosity. The SA model is particularly effective for wall-bounded flows and aerodynamic surfaces, as it directly computes the eddy viscosity without relying on multiple turbulence variables. The observed variation in turbulent viscosity between the top and bottom surfaces is well captured by the SA model, which responds sensitively to changes in shear and strain rates within the boundary layer. The thicker boundary layer on the top surface results in higher strain gradients and enhanced turbulence production, leading to elevated eddy viscosity values. This behavior aligns with the SA model formulation, where turbulent viscosity increases in regions of strong shear and near-wall turbulence. Thus, the SA model not only reflects the physical trends observed in the empirical and computational data but also reinforces the link between boundary layer growth and turbulence intensity.

4   Conclusion

This numerical investigation of the Delville shear layer demonstrates the Spalart-Allmaras turbulence model's capability to predict key flow features in a 2D mixing layer, with reasonable agreement to experimental data from Delville et al. [2]. The results highlight the model's strengths in capturing near-field velocity profiles and turbulent viscosity distributions, particularly with medium to fine mesh resolutions, which are critical for resolving turbulent mixing and velocity decay downstream. However, discrepancies in the far-field region, such as overprediction of velocity in high-speed regions and underprediction in low-speed zones, suggest limitations in the SA model's ability to fully capture anisotropic turbulence and large-scale vortical structures. The grid independence study underscores the necessity of adequate mesh refinement to achieve reliable predictions, with the medium-resolution mesh (58K cells) offering a balance between accuracy and computational efficiency. These findings contribute to the validation of the SA model for shear-dominated flows and emphasize the importance of mesh design in CFD simulations. Future work could explore higher-fidelity models, such as Large Eddy Simulation (LES), to address the observed limitations and enhance prediction accuracy in complex turbulent flows.

Acknowledgment

The author gratefully acknowledges ANSYS Inc. for providing access to the ANSYS Student Version of their simulation software. This powerful tool has been instrumental in enabling the computational modeling and analysis presented in this work. For more information regarding the ANSYS Student version, please visit the ANSYS Academic Student Portal, URL: https://www.ansys.com/en-in/academic/students.

Usage Disclaimer

The ANSYS Student Version software used in this study is licensed solely for educational and personal development purposes. It is not intended for any commercial use or financial gain. All simulations and results generated using this software comply with the terms and conditions set forth by ANSYS Inc.

Plagiarism Notice

This project is an original student work. If any part of the content appears similar to existing sources or seems like plagiarism, please notify the author. Appropriate credits and citations will be promptly added or corrected. Due to resource limitations, this work has not undergone formal plagiarism checking.

References

[1] ANSYS Inc. *ANSYS Fluent Theory Guide*. ANSYS Inc., Canonsburg, PA, release 2022 r1 edition, 2022. Available from ANSYS documentation portal.

[2] J. Delville, S. Bellin, J. H. Garem, and J. P. Bonnet. Analysis of structures in a turbulent, plane mixing layer by use of a pseudo flow visualization method based on hot-wire anemometry. In Hans-Hermann Fernholz and Heinrich E. Fiedler, editors, *Advances in Turbulence 2*, pages 251–256, Berlin, Heidelberg, 1989. Springer Berlin Heidelberg.

[3] NASA Langley Research Center. 2d mixing layer validation case, n.d. Accessed: 2025-08-08.

[4] Philippe R. Spalart and Steven R. Allmaras. A one-equation turbulence model for aerodynamic flows. In *AIAA Paper*, number 92-0439, 1992.

[5] D. C. Wilcox. Turbulence models and their application to complex flows. Technical Report NASA/TM-1998-208694, NASA Langley Research Center, 1998. Version 4.01.